



UNIVERSITAT POLITÈCNICA DE CATALUNYA
BARCELONATECH

Escola Superior d'Enginyeries Industrial,
Aeroespacial i Audiovisual de Terrassa

Advanced Aeroelasticity

Project

Numerical Aeroelastic study of the Pazy Wing

MASTER IN AERONAUTICAL ENGINEERING

Authors:

Alberto Martí, Antoni
Villalta Quintana, Gerard

Professor:

Roca Cazorla, David

Date:

January 18th, 2023

Table of Contents

Table of Contents	i
List of Figures	ii
List of Tables	ii
1 Problem Description	1
2 Virtual Experiment	3
2.1 Algorithm procedure	3
2.2 Results	4
3 Numerical Modelling	5
3.1 Mesh generation	5
3.2 Structural modelling	6
3.2.1 Stiffness matrix	6
3.2.2 Mass matrix	7
3.3 Aerodynamic modelling	9
3.4 Aeroelastic coupling	10
3.4.1 Aeroelastic coupling matrices	10
3.4.2 Inverse Aeroelastic coupling matrix	11
3.5 Static response of the structure	12
3.6 Static response of the structure with equilibrium in angle of attack	12
3.7 Computation of the Divergence velocity	12
3.8 Computation of the Flutter velocity	13
4 Results	15
4.1 Static Response	15
4.2 Divergence condition	16
4.3 Natural modes of Vibration	16
4.4 Flutter condition	17
5 Conclusions	20

List of Figures

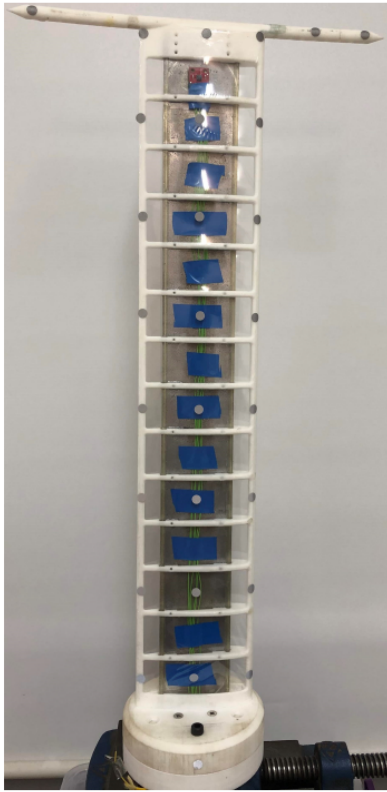
1	Pazy wing models	1
2	Pazy Wing schematic	2
3	Shear center position computed	3
4	Virtual experimental values	4
5	Numerical discretization of the structure	5
6	Cross sections of the Pazy Wing	5
7	Horseshoe element scheme	9
8	Comparison between static solution with and without aerodynamic coupling . . .	15
9	Natural modes	17
10	Natural modes	18
11	Mode's p value evolution	18

List of Tables

1	Parameters for the effective structural properties of the wing	4
2	Static tip displacement at $U_\infty = 30$ m/s	16
3	Static tip displacement at $U_\infty = 50$ m/s	16
4	Comparison of divergence free stream velocity	16
5	Natural frequencies comparison with experimental data from [2]	17
6	Comparison of test experimental free stream velocity	19

1 Problem Description

In this report the numerical study of the PazyWing will be presented. The Pazy Wing is a highly flexible wing that has been specially designed to be used as benchmark for non linear aeroelastic simulation models. This wing is made out of nylon LE, TE and ribs, a thin aluminium spar and outer skins of polyester film. The airfoil used for the model is a NACA0018 . In figure 1a it can be seen a model of this wing and in Figure 1b the same wing but deflected due to aerodynamic loads inside a wind tunnel.



(A) Instrumented wing [1]



(B) wind tunnel test of the wing [2]

FIGURE 1: Pazy wing models

In figure 2 are shown the dimensions of the Pazy wing and of its individual components. The total length is 550 mm and a chord of 100 mm. The ribs have a total thickness of 4 mm and are spaced 38.4 mm apart. As can be seen, one extreme is fixed and at the other one there is a rod attached to it that allows to add weights and change the stability of the structure.

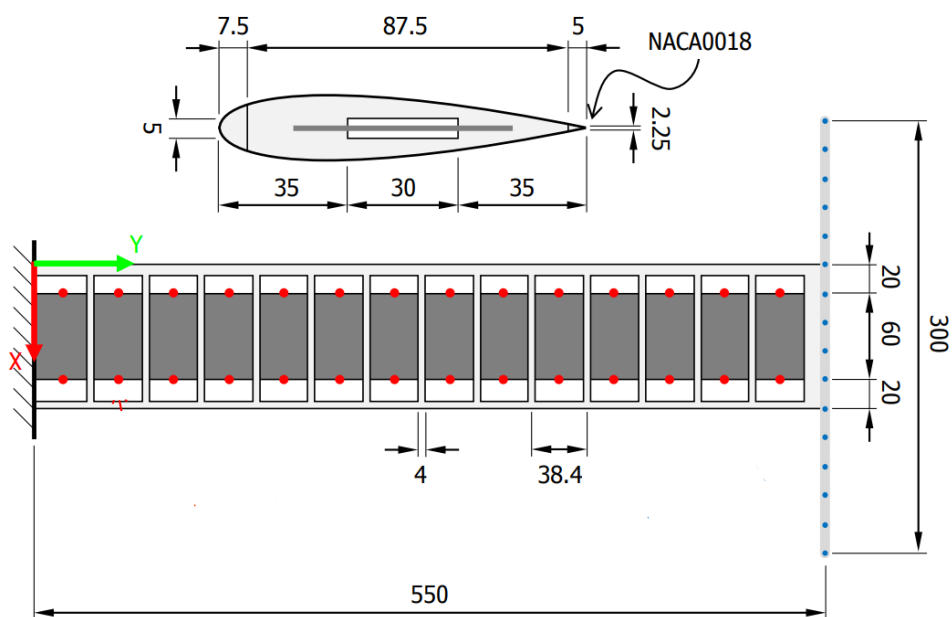


FIGURE 2: Pazy Wing schematic

2 Virtual Experiment

For the development of the numerical model of the Pazy Wing it is required to obtain the values of characteristic parameters that define the structural behaviour of the structure. This parameters are the location of the shear centre (x_{sc}) the torsional stiffness (\bar{GJ}) and the bending stiffness (\bar{EI}). The way this parameters are obtained is by conducting a virtual experiment.

2.1 Algorithm procedure

The first parameter to be obtained is the position of the shear centre. Using the code provided by the professor, several masses can be placed at different positions, obtaining the corresponding torsion displacement generated. Once the location of the shear centre is bounded between two of the predefined positions, increasing masses are placed at the two nodes in order to balance the wing and obtain null torsion. The position of the shear centre can be obtained by applying the lever rule. This process is repeated 10 times to account for random variability, and it is performed at each section in order to check if the value of shear centre remains constant along the wing:

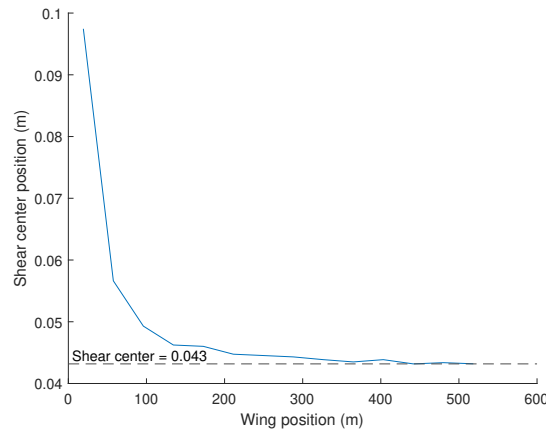


FIGURE 3: Shear center position computed

It can be seen how the values at the root are much more higher than the ones obtained at the tip. This can be explained due to the accuracy of the convergence method. The lower torsion generated at the root affects the equilibrium forces, causing a much higher variability in the mass values. Thus, the final value taken as shear center position is the value at the tip.

Once the shear centre is found, the next step is to assign a mass at any position and obtain the displacement at each sensor location. With that, the deformation profile can be obtained by fitting a first order polynomial for torsion and a third order polynomial for bending. The torsional and flexural rigidities can be computed as:

$$\bar{GJ} = \frac{F(x_{sc} - x)}{a_1}; \quad \bar{EI} = -\frac{F}{6b_3} \quad (1)$$

Where a_1 and b_3 are the coefficients of the linear and cubic elements of the corresponding torsion and bending polynomial fitting. The same way as in the shear centre, this process is repeated 10 times and with different mass values for each mass node position. In this way, any random variation or model inaccuracy can be detected and eliminated by averaging all the values.

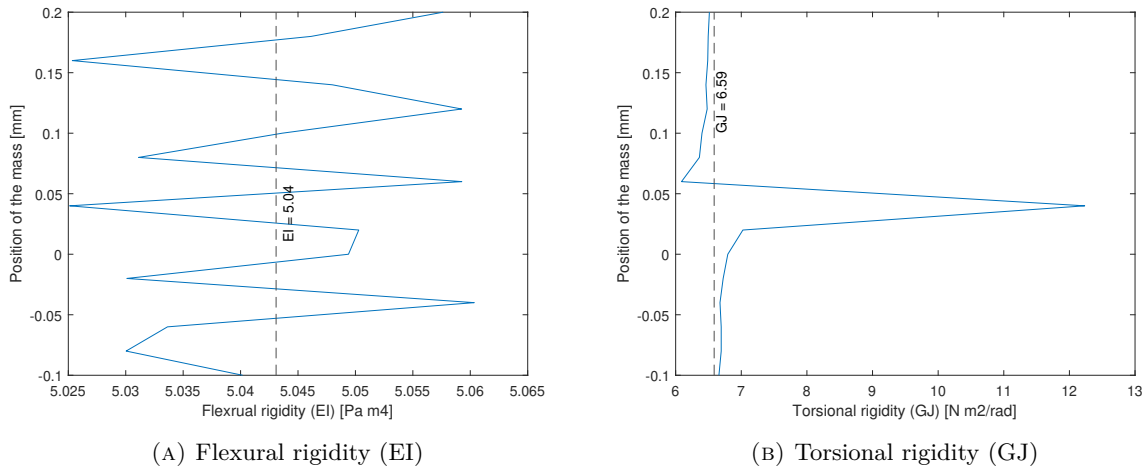


FIGURE 4: Virtual experimental values

Checking the results for flexural rigidity, certain variability can be observed. This variability has been assessed and it does not represent any implication with values with precision of 2 decimals. For the torsional rigidity, an spike appears in the exact location of the shear center, where the torsion function slope is equal to 0 causing an asymptote in the equation 2.1. After removing this point, as well as in the previous value, the variability observed had not effect within the first 2 decimals.

2.2 Results

The following parameters are obtained by running the previous algorithm:

TABLE 1: Parameters for the effective structural properties of the wing

Description	Symbol	Value	Units
Shear center	\bar{x}_{sc}	43	%
Bending Stiffness	\bar{EI}	5.04	Nm^2
Torsional Stiffness	\bar{GJ}	6.59	Nm^2

3 Numerical Modelling

Once the parameters x_{sc} , \bar{EI} and \bar{GJ} are obtained from the virtual experiment, the numerical model of the Pazy Wing can be implemented. This step has been guided in its majority, but the final implementation of the model and global algorithm has been left open to allow to implement different models.

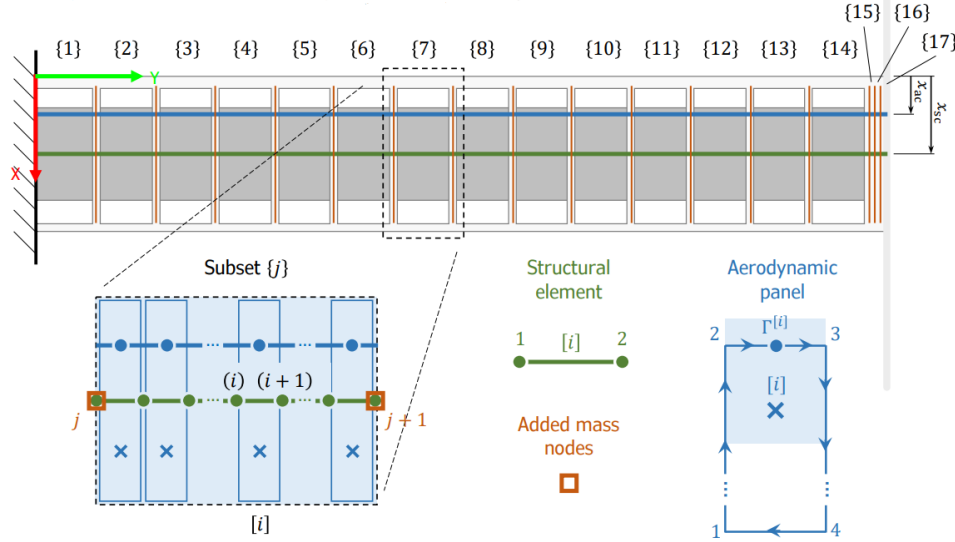


FIGURE 5: Numerical discretization of the structure

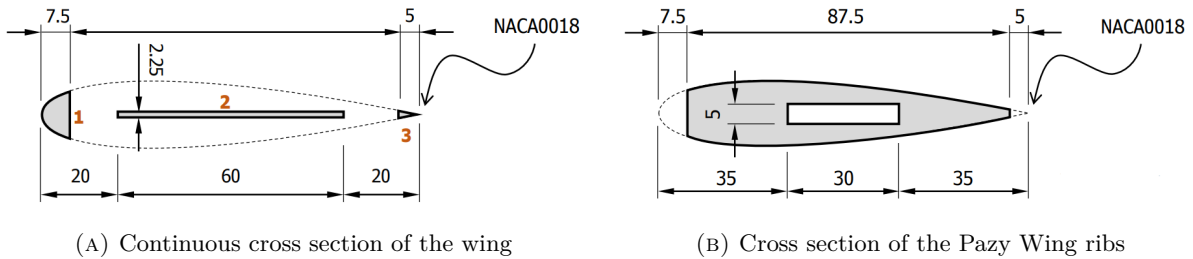


FIGURE 6: Cross sections of the Pazy Wing

3.1 Mesh generation

The first step consist on generating the elements that define our mesh. The scheme presented on Figure 5 represents the layout to be implemented. Starting from the different sections provided by the assignment statement, each of them are divided in 5 smaller elements, even the shorter sections at the wing tip. Each element is characterised by two nodes for the structural element and a horseshoe panel for the aerodynamic model.

Once the nodes position are defined, the connectivity table for the elements is created. In addition, another connectivity table is created to define the sections, information that will be used in the structural computation.

3.2 Structural modelling

The next step taken to develop the aeroelastic model is the definition of the structural matrices related to stiffness (K) and mass (M). This matrices were already generated using the Euler-Bernoulli beam theory and provided by the professor, but some sections parameters were needed to assemble them.

3.2.1 Stiffness matrix

The stiffness matrix is obtained from assembling the elemental stiffness matrices defined for each beam element. The elastic response is divided between torsion and bending, obtaining two different matrices which are added to the corresponding global degrees of freedom of the element:

$$K = K + K_b + K_t \quad (2)$$

$$\begin{aligned} \left[\mathbf{K}_t^{[i]} \right] &= \frac{\overline{GJ}^{[i]}}{l} \begin{bmatrix} 1 & 0 & 0 & -1 & 0 & 0 \\ 0 & 0 & 0 & 0 & 0 & 0 \\ 0 & 0 & 0 & 0 & 0 & 0 \\ -1 & 0 & 0 & 1 & 0 & 0 \\ 0 & 0 & 0 & 0 & 0 & 0 \\ 0 & 0 & 0 & 0 & 0 & 0 \end{bmatrix} \\ \left[\mathbf{K}_b^{[i]} \right] &= \frac{\overline{EI}}{(l^{[i]})^3} \begin{bmatrix} 0 & 0 & 0 & 0 & 0 & 0 \\ 0 & 12 & 6l^{[i]} & 0 & -12 & 6l^{[i]} \\ 0 & 6l^{[i]} & 4(l^{[i]})^2 & 0 & -6l^{[i]} & 2(l^{[i]})^2 \\ 0 & 0 & 0 & 0 & 0 & 0 \\ 0 & -12 & -6l^{[i]} & 0 & 12 & -6l^{[i]} \\ 0 & 6l^{[i]} & 2(l^{[i]})^2 & 0 & -6l^{[i]} & 4(l^{[i]})^2 \end{bmatrix} \end{aligned} \quad (3)$$

All the parameters needed to compute the matrices are the experimental values for torsional and flexural rigidity, as well as the length of the element. Thus, no calculations are needed.

3.2.2 Mass matrix

The mass matrix, similar to the stiffness matrix, is also divided for each element between torsion and bending response. The provided matrices can be found in 4

$$\begin{aligned} [\mathbf{M}'_t] &= \frac{I_{cm}l}{6} l^{[i]} \begin{bmatrix} 2 & 0 & 0 & 1 & 0 & 0 \\ 0 & 0 & 0 & 0 & 0 & 0 \\ 0 & 0 & 0 & 0 & 0 & 0 \\ 1 & 0 & 0 & 2 & 0 & 0 \\ 0 & 0 & 0 & 0 & 0 & 0 \\ 0 & 0 & 0 & 0 & 0 & 0 \end{bmatrix} \\ [\mathbf{M}'_b] &= \frac{\overline{\rho A} l^{[i]}}{420} \begin{bmatrix} 0 & 0 & 0 & 0 & 0 & 0 \\ 0 & 156 & 22l^{[i]} & 0 & 54 & -13l^{[i]} \\ 0 & 22l^{[i]} & 4(l^{[i]})^2 & 0 & 13l^{[i]} & -3(l^{[i]})^2 \\ 0 & 0 & 0 & 0 & 0 & 0 \\ 0 & 54 & 13l^{[i]} & 0 & 156 & -22l^{[i]} \\ 0 & -13l^{[i]} & -3(l^{[i]})^2 & 0 & -22l^{[i]} & 4(l^{[i]})^2 \end{bmatrix} \end{aligned} \quad (4)$$

In this case, some calculations must be done in order to obtain the necessary physical properties of the beam element section. To do so, the section's parts has been divided in different rectangular elements¹ and their properties computed and added:

- Linear density ($\overline{\rho A}$)

$$\overline{\rho A} = \sum_{j=1}^{n_{el}} \rho^{[j]} b^{[j]} h^{[j]} \quad (5)$$

$$b^{[j]} = x(j+1) - x(j), \quad h^{[j]} = 2(y(j+1) + y(j))/2$$

- Center of mass (x_{cm})

$$x_{cm} = \frac{1}{\overline{\rho A}} \sum_{j=1}^{n_{el}} \rho^{[j]} A^{[j]} x_{cm}^{[j]} \quad (6)$$

$$A^{[j]} = bh, \quad x_{cm}^{[j]} = (x(j+1) + x(j))/2$$

- Inertia at center of mass (z-axis) (I_{cm})

$$I_{cm} = \sum_{j=1}^{n_{el}} \rho^{[j]} (I_z^{[j]} + A^{[j]} (x_{cm} - x_{cm}^{[j]})^2) \quad (7)$$

$$I_z^{[j]} = hb^3/12$$

This matrices are computed using the center of mass as reference point. Thus, a translation to the shear center must be applied by using equation 8

$$M = M + [d]^T ([M_b + M_t]) [d] \quad (8)$$

¹The aluminium plate with rectangular section can be computed as a unique rectangular element and added to the other ones

Where matrix $[d]$ is:

$$[d] = \begin{bmatrix} 1 & 0 & 0 & 0 & 0 & 0 \\ -d & 1 & 0 & 0 & 0 & 0 \\ 0 & 0 & 1 & 0 & 0 & 0 \\ 0 & 0 & 0 & 1 & 0 & 0 \\ 0 & 0 & 0 & -d & 1 & 0 \\ 0 & 0 & 0 & 0 & 0 & 1 \end{bmatrix} \quad (9)$$

Where variable d is the distance between center of mass and shear center ($d = x_{cm} - x_{sc}$).

In addition to the previous matrices, some punctual masses must be added to account for the nylon ribs of the model built. To do so, the following matrix is added to the mass matrix at the corresponding degrees of freedom of each node with rib:

$$[M_r] = h^r \begin{bmatrix} I_{cm}^r + \rho^r A^r (x_{cm}^r - x_{sc})^2 & -\rho^r A^r (x_{cm}^r - x_{sc}) & 0 \\ -\rho^r A^r (x_{cm}^r - x_{sc}) & \rho^r A^r & 0 \\ 0 & 0 & I_x^r \end{bmatrix} \quad (10)$$

In this case, similar parameters will be computed using the same approach as in the previous case.

- Area (A^r)

$$A^r = \sum_{j=1}^{n_{el}} A^{[j]} \quad (11)$$

$$A^{[j]} = bh$$

- Center of mass (x_{cm}^r)

$$x_{cm}^r = \sum_{j=1}^{n_{el}} A^{[j]} x_{cm}^{[j]} \quad (12)$$

$$x_{cm}^{[j]} = (x(j+1) + x(j))/2$$

- Inertia from center of mass (z-axis) (I_{cm}^r)

$$I_{cm}^r = \sum_{j=1}^{n_{el}} \rho (I_z^{[j]} + A^{[j]} (x_{cm}^r - x_{cm,el}^{[j]})^2) \quad (13)$$

$$I_z^{[j]} = hb^3/12$$

- Inertia from origin (x-axis) (I_x^r)

$$I_x^r = \sum_{j=1}^{n_{el}} \rho (I_x^{[j]} + A^{[j]} (x_{cm}^r - x_{cm}^{[j]})^2) \quad (14)$$

$$I_x^{[j]} = bh^3/12$$

In this case, the rectangular elements can take into account the slot and divide the domain in three different regions. Nevertheless, it is much more simpler to compute the hole rib and then subtract the slot by deducing from each parameter the corresponding rectangular slot element value.

3.3 Aerodynamic modelling

Once the structural model is created, it is time to develop the aerodynamic model for our wing, based on Prandtl Lifting-line theory. To do so, the finite elements created are modelled as horseshoe elements with determined aerodynamic center and collocation as shown in figure 7.

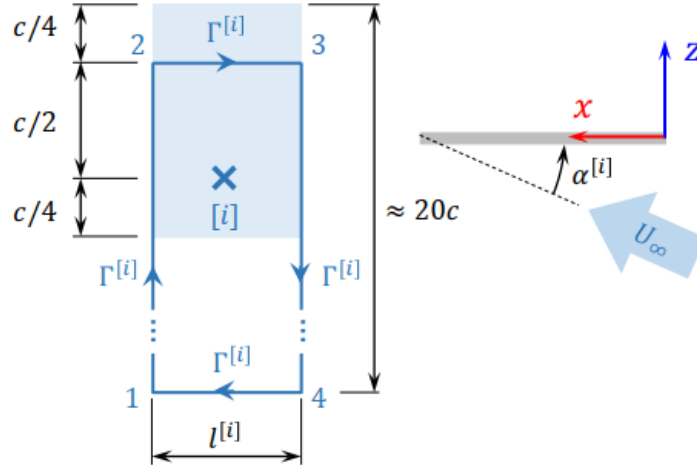


FIGURE 7: Horseshoe element scheme

Applying the Kutta condition at the collocation points of each element, the following equation is obtained:

$$\left(\sum_{j=1}^n \left(\mathbf{v}_{12}^{[j]} + \mathbf{v}_{23}^{[j]} + \mathbf{v}_{34}^{[j]} \right) \Big|_{\mathbf{x}=\mathbf{x}^{[i]}} + \mathbf{U}_{\infty} \right) \cdot \mathbf{n}^{[i]} = 0 \quad (15)$$

$$\mathbf{v}_{jk}^{[i]}(\mathbf{x}) = \frac{\Gamma^{[i]}}{4\pi} \frac{\mathbf{r}_j \times \mathbf{r}_k}{\|\mathbf{r}_j \times \mathbf{r}_k\|^2} \left(\frac{\mathbf{l}^{[i]} \cdot \mathbf{r}_j}{\|\mathbf{r}_j\|} - \frac{\mathbf{l}^{[i]} \cdot \mathbf{r}_k}{\|\mathbf{r}_k\|} \right); \quad \mathbf{r}_j = \mathbf{x} - \mathbf{x}_j; \quad \mathbf{l}^{[i]} = \mathbf{x}_k - \mathbf{x}_j$$

Where x are the coordinates of the collocation point and x_k and x_j the initial and final coordinates of the vortex lines.

Rearranging the previous expression in a matrix equation:

$$\mathbf{A}\mathbf{\Gamma} = -U_{\infty}\mathbf{\alpha} \quad (16)$$

Where matrix \mathbf{A} correspond to the different influence coefficients between the elements. The value of each element can be computed with the equation 17.

$$A_{ij} = \left(\mathbf{v}_{12}^{[j]}(\mathbf{x}^{[i]}) + \mathbf{v}_{23}^{[j]}(\mathbf{x}^{[i]}) + \mathbf{v}_{34}^{[j]}(\mathbf{x}^{[i]}) \right) \Big|_{\Gamma^{[j]}=1} \cdot \mathbf{n}^{[i]} \quad (17)$$

Finally, by developing the lift equation and introducing the previous obtained matrices, the final expression for the lift force is:

$$L^{[i]} = \rho_{\infty} U_{\infty} l^{[i]} \Gamma^{[i]} \rightarrow \{\mathbf{L}\} = -\rho_{\infty} U_{\infty}^2 [\mathbf{S}][\mathbf{A}]^{-1} \{\mathbf{\alpha}\}; \quad [\mathbf{S}] = \begin{bmatrix} l_{[1]} & & 0 \\ & \ddots & \\ 0 & & l^{[n_{el}]} \end{bmatrix} \quad (18)$$

3.4 Aeroelastic coupling

The aeroelastic coupling matrices are the elements that connect the structural model with the aerodynamic model. There are 4 matrices involved in this coupling process, the 3 $I_{\alpha u}$ matrices and the I_{fL} matrix.

3.4.1 Aeroelastic coupling matrices

Starting with the $I_{\alpha u}$, this matrix is used interpolate the value of the angle of attack (α) from the value of the DOFs at the adjacent structural nodes.

For this project, the quasi steady aerodynamic model has been selected. This one is shown in expression 19.

$$l^{[i]} = q_{\infty} c C_{l,\alpha} \alpha^{[i]} \quad \text{where} \quad \alpha^{[i]} = \left(\theta^{[i]} - \frac{\dot{w}_{sc}^{[i]}}{U_{\infty}} \right) \quad (19)$$

Then, the angle of attack α at the centre of each panel has to be interpolated from the value of the DOFs at the adjacent structural nodes. To do it the shape functions shown in 20 and 21 will be used for each one of the structural DOFs (θ, w_{sc} and γ).

$$\begin{aligned} \theta^{[i]}(\xi) &= N_{\theta}^{(1)}(\xi) \theta^{(i)} + N_{\theta}^{(2)}(\xi) \theta^{(i+1)} \\ w_{sc}^{[i]}(\xi) &= N_w^{(1)}(\xi) w_{sc}^{(i)} + \frac{l^{[i]}}{2} N_{\gamma}^{(1)}(\xi) \gamma^{(i)} + N_w^{(2)}(\xi) w_{sc}^{(i+1)} + \frac{l^{[i]}}{2} N_{\gamma}^{(2)}(\xi) \gamma^{(i+1)} \\ \gamma^{[i]}(\xi) &= N_{w,\xi}^{(1)}(\xi) w_{sc}^{(i)} + \frac{2}{l^{[i]}} N_{\gamma,\xi}^{(1)}(\xi) \gamma^{(i)} + N_{w,\xi}^{(2)}(\xi) w_{sc}^{(i+1)} + \frac{2}{l^{[i]}} N_{\gamma,\xi}^{(2)}(\xi) \gamma^{(i+1)} \end{aligned} \quad (20)$$

$$\begin{aligned} N_{\theta}^{(1)}(\xi) &= \frac{1}{2}(1 - \xi) & N_w^{(1)}(\xi) &= \frac{1}{4}(2 - 3\xi + \xi^3) & N_{\gamma}^{(1)}(\xi) &= \frac{1}{4}(1 - \xi - \xi^2 + \xi^3) \\ N_{\theta}^{(2)}(\xi) &= \frac{1}{2}(1 + \xi) & N_w^{(2)}(\xi) &= \frac{1}{4}(2 + 3\xi - \xi^3) & N_{\gamma}^{(2)}(\xi) &= \frac{1}{4}(-1 - \xi + \xi^2 + \xi^3) \\ \xi &= \frac{2y - (y^{(i)} + y^{(i+1)})}{y^{(i+1)} - y^{(i)}} \end{aligned} \quad (21)$$

Considering the system of equations of motion shown in 22, the $I_{\alpha u}^{(0)}$ it is used to compute the contribution to the angle of attack that the aerodynamic panel sees from the static $\{u\}$, $I_{\alpha u}^{(1)}$ from $\{\dot{u}\}$ and $I_{\alpha u}^{(2)}$ from $\{\ddot{u}\}$. With this in mind and recovering equation 19, for this numerical model the matrix full of zeros $I_{\alpha u}^{(2)} = [0]$.

$$[M]\{\ddot{u}\} + [C]\{\dot{u}\} + [K]\{u\} = \{f\} \quad (22)$$

The angle of attack would be expressed as shown in equation 23. Then, recovering equation 19, 20 and 21, $I_{\alpha u}^{(2)}$ would be expressed for a generic element as shown in equation 24, $I_{\alpha u}^{(1)}$ as in 25

and $I_{\alpha u}^{(0)}$ as in 26.

$$\alpha^{[i]} = [I_{\alpha u}^{(2)}]\{\ddot{u}^{[i]}\} + [I_{\alpha u}^{(1)}]\{\dot{u}^{[i]}\} + [I_{\alpha u}^{(0)}]\{u^{[i]}\} \quad \text{where} \quad \{\mathbf{u}^{[i]}\} = \begin{Bmatrix} \theta^{(i)} \\ w_{Sc}^{(i)} \\ \gamma^{(i)} \\ \theta^{(i+1)} \\ w_{Sc}^{(i+1)} \\ \gamma^{(i+1)} \end{Bmatrix} \quad (23)$$

$$[I_{\alpha u}^{(2)}] = [0 \quad 0 \quad 0 \quad 0 \quad 0 \quad 0] \quad (24)$$

$$[I_{\alpha u}^{(1)}] = \frac{-1}{U_{\infty}} \begin{bmatrix} 0 & N_w^{(1)}(0) & \frac{l^{[i]}}{2} N_{\gamma}^{(1)}(0) & 0 & N_w^{(2)}(0) & \frac{l^{[i]}}{2} N_{\gamma}^{(2)}(0) \end{bmatrix} \quad (25)$$

$$[I_{\alpha u}^{(0)}] = \begin{bmatrix} N_{\theta}^{(1)}(0) & 0 & 0 & N_{\theta}^{(2)}(0) & 0 & 0 \end{bmatrix} \quad (26)$$

Finally, all previous matrices are computed for each element and assembled in the corresponding global aeroelastic coupling matrices. Each elemental matrix is assembled in the row corresponding to the element and the columns related to the element's nodes degrees of freedom.

3.4.2 Inverse Aeroelastic coupling matrix

This matrix is similar to the $I_{\alpha u}$ but it is used to transform the aerodynamic lift forces to the forces and moments at the structural nodes. The virtual work of an external distributed force per unit length can be expressed as in equation 27.

$$\delta W^{\text{ext}} = \sum_{i=1}^n \int_{y^{(i)}}^{y^{(i+1)}} \delta u_z f_z dx \quad (27)$$

Changing the expression of the distributed force by the the equivalent considering discrete values at the node as $f_z = F^{[i]} \delta(y - y^{[i]})$ where $\delta(y)$ is the Dirac delta leads to expression 28.

$$\delta W^{\text{ext}} = \sum_{i=1}^n \delta u_z(y^{[i]}) F^{[i]} = \sum_{i=1}^n \left(\delta w_{sc}(y^{[i]}) - (x - x_{sc}) \delta \theta(y^{[i]}) \right) F^{[i]} \quad (28)$$

In expression 28, $\delta \theta(y^{[i]})$ and $\delta w_{sc}(y^{[i]})$ are evaluated at the centre of the aerodynamic panel. Developing the expression for one element using the shape functions 20, the following equation can be obtained:

$$\begin{aligned} \delta W_{[i]}^{\text{ext}} = & \left(N_w^{(1)}(0) \underbrace{w_{sc}^{[i]}}_c + \frac{l}{2} N_{\gamma}^{(1)}(0) \underbrace{\gamma^{[i]}}_c + N_w^{(2)}(0) \underbrace{w_{sc}^{[i+1]}}_c + \frac{l}{2} N_{\gamma}^{(2)}(0) \underbrace{\gamma^{[i+1]}}_c \dots \right. \\ & \left. \dots - \underbrace{(x_{ac} - x_{sc})}_e N_{\theta}^{(1)}(0) \underbrace{\theta^{[i]}}_c - \underbrace{(x_{ac} - x_{sc})}_e N_{\theta}^{(2)}(0) \underbrace{\theta^{[i+1]}}_c \right) L^{[i]} \end{aligned} \quad (29)$$

Where c are the trial functions resulting from the structural finite element model. Removing those terms (the same is done for the stiffness and mass matrix obtention) the virtual work is equal to the force vector and rearranging the terms in a matrix position, the elemental inverse aeroelastic coupling matrix is obtained:

$$[I_{fL}] = \begin{bmatrix} -eN_{\theta}^{(1)}(0) & N_w^{(1)}(0) & \frac{l}{2}N_{\gamma}^{(1)}(0) & -eN_{\theta}^{(2)}(0) & N_w^{(2)}(0) & \frac{l}{2}N_{\gamma}^{(1)}(0) \end{bmatrix}^T \quad (30)$$

Finally, this case must be assembled. Nevertheless, the dimensions are transposed so the vector obtained must be assembled at the column corresponding to the element and the rows related to the degrees of freedom.

3.5 Static response of the structure

After defining all the necessary matrices, some initial calculations can be performed in order to obtain some initial checks. Thus, evaluating the static response of the wing under some constant force distribution (initial aerodynamic lift for a determined angle of attack) the magnitude of the obtained displacement can help us to detect possible errors. To do so, the following force matrix has been assembled:

$$\{f\} = [I_{fL}]\{L\} = [I_{fL}](-(U_{\infty})^2\rho_{\infty}[S][A]^{-1}\{\alpha\}) \quad (31)$$

Then, applying the Dirichlet boundary conditions at the root of the wing (all degrees of freedom set to 0 except the elastic twist that is equal to α), the static response of the system can be computed as:

$$\{u(I_f, 1)\} = [K(I_f, I_f)]^{-1}([f(I_f, 1)] - [K(I_f, I_p)]\{u(I_p, 1)\}) \quad (32)$$

3.6 Static response of the structure with equilibrium in angle of attack

Computing the static response of the system is one thing, but that does not necessarily mean that at the first iteration the system will be at equilibrium. Imposing a uniform distribution of angle of attack along the wing will result in a change of twist, thus changing the lift distribution that initially has been calculated. To find the static deflection of the wing under equilibrium of angle of attack and elastic twist the next algorithm has been implemented:

1. Define the U_{∞} and α
2. Compute the the boundary conditions with first node of the structure having an initial twist equal to the angle of attack. $U_p(1, :) = [\alpha \quad 1 \quad 1]$
3. Compute the initial lift distribution as $\{f\} = [I_{fL}](-(U_{\infty})^2\rho_{\infty}[S][A]^{-1}\{\alpha\})$
4. Compute value of the free DOFs: $\{u(I_f, 1)\} = [K(I_f, I_f)]^{-1}([f(I_f, 1)] - [K(I_f, I_p)]\{u(I_p, 1)\})$
5. Compute the new distribution of angle of attack as: $\alpha^{new} = I\alpha u^{(0)}u$
6. If $\max(\alpha^{new} - \alpha) > 10^6$, make $\alpha = \alpha^{new}$ and go back to **3**. Else go to next step
7. Return u and finish loop.

3.7 Computation of the Divergence velocity

The condition for the divergence velocity is the minimum dynamic pressure \hat{q} that makes $\det([\bar{K}_{eff}(\hat{q})]) = 0$. The effective stiffness matrix is a combination of the structural stiffness matrix ($[K_s]$) and the aerodynamic stiffness matrix ($[K_a]$), then the condition of divergence can be rewritten as in expression 33. Here the matrix $[A]$ is the aerodynamic influence coefficients

matrix and the $[S]$ is a diagonal matrix containing the width of each aerodynamic panel.

$$\det([K_s] - \hat{q}[K_a]) = \quad \text{where} \quad [K_a] = [I_{fL}][S][A]^{-1}[I_{\alpha u}^{(0)}] \quad (33)$$

Since $\det([\bar{K}_{eff}(\hat{q})]) = \Pi_i \lambda_i$, where λ_i are the eigenvalues of the matrix \bar{K}_{eff} . If one of the eigenvalues is a 0 then the determinant will be also 0. The problem can be rearranged as a eigenvalue problem as expressed in equation 34.

$$(\bar{K}_{eff}(\hat{q}) - \lambda_i[1]) \{\theta\} = \{0\} \longrightarrow ([K_a]^{-1} [K_s] - (\hat{q} + \lambda_i) [1]) \{\theta\} = \{0\} \quad (34)$$

The eigenvalues of the matrix $[K_a]^{-1} [K_s] \lambda'_i$ will be equal to $\hat{q} + \lambda_i$. The condition for divergence corresponds to the minimum \hat{q} that makes $\lambda_i = 0$, then the final divergence condition the one shown in expression 35.

$$\hat{q}_D = \min(\lambda'_i > 0) \longrightarrow U_{\infty,D} = \sqrt{\frac{\hat{q}_D}{\rho_{\infty}}} \quad (35)$$

The previous approach is possible if $[K_a]$ is invertable, and in the present case it isn't. The problem can still be solved but instead of inverting the aerodynamic stiffness matrix, the structural stiffness matrix will be inverted in its place. Then the divergence condition can still be found by solving equation 36 and 37.

$$(\bar{K}_{eff}(\hat{q}) - \lambda_i[1]) \{\theta\} = \{0\} \longrightarrow ([K_a] [K_s]^{-1} - \left(\frac{1}{\hat{q}} + \lambda_i\right) [1]) \{\theta\} = \{0\} \quad (36)$$

$$\hat{q}_D = \frac{1}{\max(\lambda'_i)} \longrightarrow U_{\infty,D} = \sqrt{\frac{\hat{q}_D}{\rho_{\infty}}} \quad (37)$$

3.8 Computation of the Flutter velocity

For the present project, the flutter condition will be evaluated using the *p method*. The steps to implement this method will be explained next. First a range of free stream velocities U_{∞} will be defined at which the system will be evaluated to. For each free stream velocity, first the effective mass and stiffness matrices are evaluated as in 38.

$$\begin{aligned} [M_{eff}(U_{\infty})] &= [M] - U_{\infty}^2 \rho_{\infty} [I_{fL}][S][A]^{-1}[I_{\alpha u}^{(2)}(U_{\infty})] \\ [C_{eff}(U_{\infty})] &= -U_{\infty}^2 \rho_{\infty} [I_{fL}][S][A]^{-1}[I_{\alpha u}^{(1)}(U_{\infty})] \\ [K_{eff}(U_{\infty})] &= [M] - U_{\infty}^2 \rho_{\infty} [I_{fL}][S][A]^{-1}[I_{\alpha u}^{(0)}(U_{\infty})] \end{aligned} \quad (38)$$

Next the each effective matrix can be reduced using the most relevant mode shapes Φ of the matrix $[M]^{-1}[K]$, obtaining the reduced matrices as shown in equation 39.

$$\begin{aligned}
 [\tilde{M}_{eff}(U_\infty)] &= [\Phi]^T [M_{eff}(U_\infty)] [\Phi] \\
 [\tilde{C}_{eff}(U_\infty)] &= [\Phi]^T [C_{eff}(U_\infty)] [\Phi] \\
 [\tilde{K}_{eff}(U_\infty)] &= [\Phi]^T [K_{eff}(U_\infty)] [\Phi]
 \end{aligned} \tag{39}$$

With this reduced matrices, a first order linearization of system can be defined as shown in 40.

$$\begin{bmatrix} \tilde{C}^{eff}(U_\infty) & \tilde{M}^{eff}(U_\infty) \\ -\mathbf{1} & \mathbf{0} \end{bmatrix} \begin{Bmatrix} \dot{\mathbf{q}} \\ \ddot{\mathbf{q}} \end{Bmatrix} + \begin{bmatrix} \tilde{K}^{eff}(U_\infty) & \mathbf{0} \\ \mathbf{0} & \mathbf{1} \end{bmatrix} \begin{Bmatrix} \mathbf{q} \\ \dot{\mathbf{q}} \end{Bmatrix} = \begin{Bmatrix} \mathbf{0} \\ \mathbf{0} \end{Bmatrix} \tag{40}$$

This system becomes unstable when the real part of one of its eigenvalues becomes positive. From the eigenvalues λ_i of the matrix 41 the p value (eigenvalues of the linearization system) of each one of them can be calculated as $p_i = -1/\lambda_i$

$$[\mathbf{D}'(U_\infty)] = \begin{bmatrix} \tilde{K}^{eff}(U_\infty)^{-1} \tilde{C}^{eff}(U_\infty) & \tilde{K}^{eff}(U_\infty)^{-1} \tilde{M}^{eff}(U_\infty) \\ -\mathbf{1} & \mathbf{0} \end{bmatrix} \tag{41}$$

At each free stream velocity U_∞ the $\max(p_i)$ is calculated. The flutter velocity (U_∞^f) will be that one that makes $\max(p_i) = 0$.

4 Results

Using the Numerical model of the Pazy Wing, 4 different studies have been performed to study the behaviour of the structure. First, the results for the static response of the structure and the divergence condition will be explained. Next, the dynamics of the system will be analysed, as the natural modes of vibration and the flutter condition.

4.1 Static Response

The first study performed is regarding the static deformation of the structure. This has been carried out with two different methods, without equilibrium of the angle of attack and with it. In figure 8 it can be see the deformed structure when a aerodynamic force associated with a uniform angle of attack of 5 deg · at $U_\infty = 30 \text{ m/s}$ compared against the same structure under the same aerodynamic conditions, but updating the aerodynamic forces with the change in elastic twist until the solution reaches an equilibrium. As can be seen, the solution with the aerodynamic coupling leads to larger vertical deformations and larger twist at the tip.

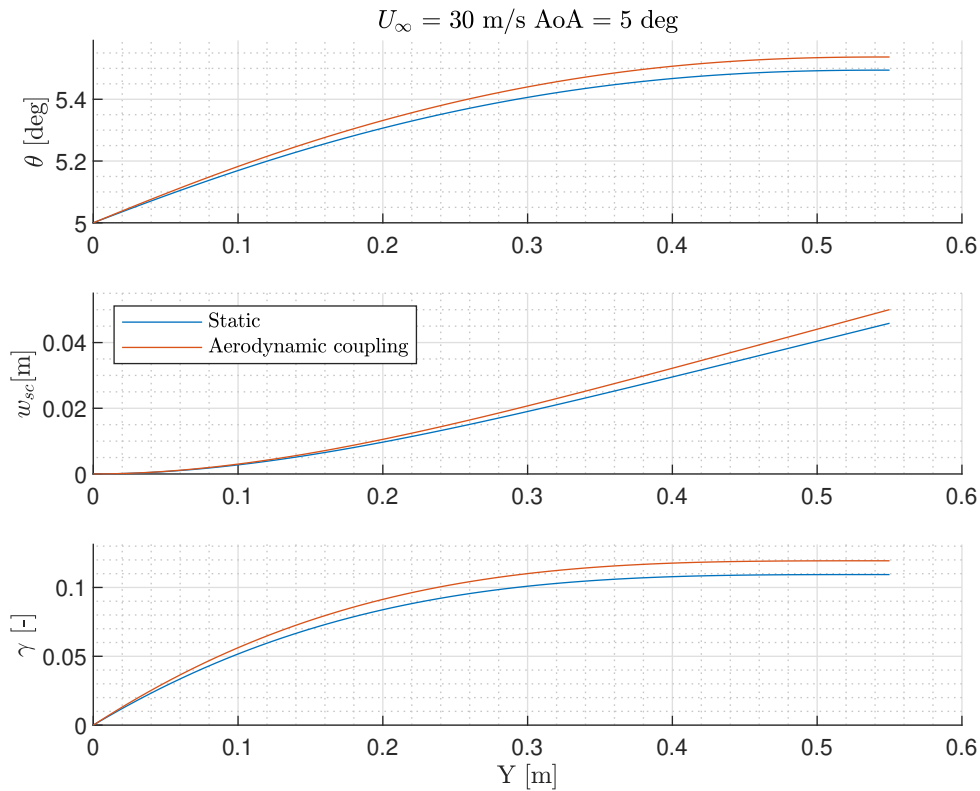


FIGURE 8: Comparison between static solution with and without aerodynamic coupling

In table 2 and 3 is shown a comparison of how the deformations are faster with the aerodynamic coupling than with the static solution alone. This effect is enhanced by the free stream velocity, the larger the speed the greater are the deformations relative to the static solution.

TABLE 2: Static tip displacement at $U_\infty = 30$ m/s

	$U_\infty = 30$ m/s			
AoA [deg]	5		10	
	Static	Aero-coupling	Static	Aero-coupling
θ^{tip} [deg]	5.49	5.54	10.99	11.07
w_{sc}^{tip} [m]	4.59E-02	5.00E-02	9.18E-02	1.00E-01
γ^{tip} [-]	1.09E-01	1.19E-01	2.19E-01	2.39E-01

TABLE 3: Static tip displacement at $U_\infty = 50$ m/s

	$U_\infty = 50$ m/s			
AoA (deg)	5		10	
	Static	Aero-coupling	Static	Aero-coupling
θ^{tip} [deg]	6.37	6.76	12.75	13.52
w_{sc}^{tip} [m]	1.27E-01	1.65E-01	2.55E-01	3.30E-01
γ^{tip} [-]	3.04E-01	3.95E-01	6.08E-01	7.89E-01

4.2 Divergence condition

As explained in section 3.7, the free stream velocity that triggers divergence condition has been calculated using the eigenvalues of the matrix $[K_a]^{-1}[K_s]$. In table 4 are shown compared against the results obtained using the ZERO aeroelastic software. As can be seen the calculated divergence velocity is about the same order as the one from the literature, but still a 30% higher.

TABLE 4: Comparison of divergence free stream velocity

	Calculated	ZAERO software[1]
U_∞^D [m/s]	107.78	83.00

4.3 Natural modes of Vibration

The first step into studying a dynamic system is to check what are the natural modes of vibration. In figure 9 the first 6 mode shapes of the Pazy Wing are shown. As can be seen, the first mode is a flapping motion (only exiting w_{sd}). The second one is the same but 2^{nd} order, with two peaks. Then the 3rd mode is exiting the elastic twist. The fourth and fifth modes are the 3^{rd} and 4^{th} order flapping. Lastly, the sixth mode is also torsional but second order.

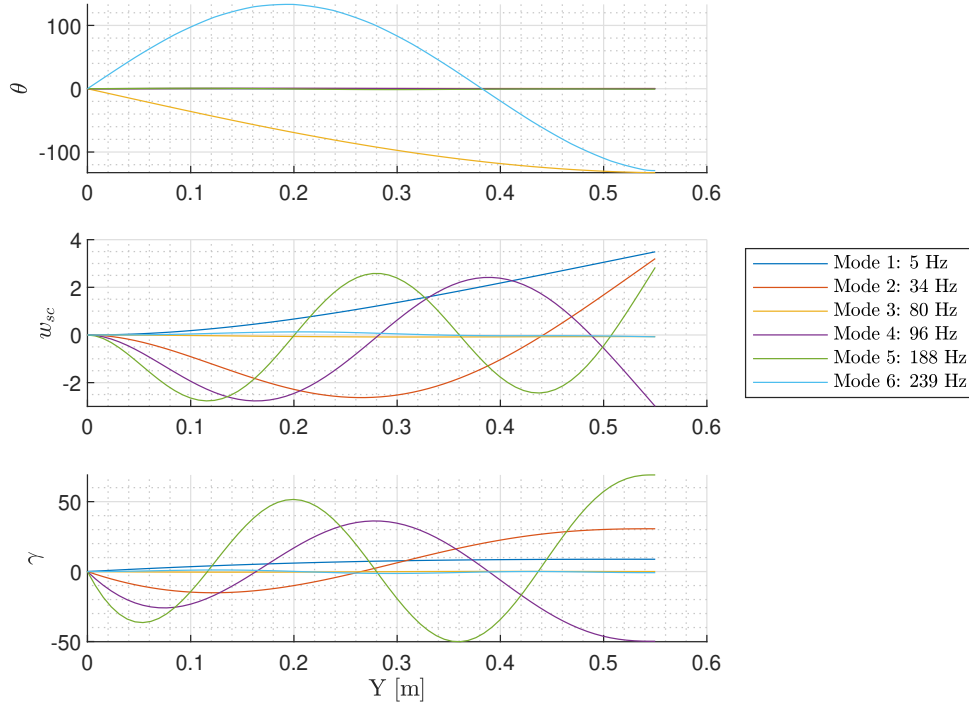


FIGURE 9: Natural modes

In table 5 it is shown a comparison of the 5 first natural frequencies between the numerical model and the experimental results. As can be seen, the first two modes seem to match reasonably well considering that structural model is linear. However, From the third mode on, the experimental results show some natural frequencies that would be between the second and third calculated modes. Then the fifth mode coincides up to some extend with the third mode of the calculated frequencies. This differences between results have to be due to the simplifications of the models used for the numerical implementation of the Pazy Wing

TABLE 5: Natural frequencies comparison with experimental data from [2]

	Numerical model	Experimental[2]
Mode	Freq [Hz]	Freq [Hz]
1	5.36	4.26
2	33.91	28.50
3	79.73	42.00
4	95.54	60.70
5	188.16	81.50

4.4 Flutter condition

The last study that has been carried out is the study of the triggering condition for flutter. In this case, the results have been computed using the p method and reducing the model with the first 6 natural modes. The evolution of the largest real part of the p values is shown in figure 10. As can be seen the system starts stable until a free stream velocity of 18.21 m/s when the flutter gets triggered and the maximum real p value becomes positive, making the system unstable.

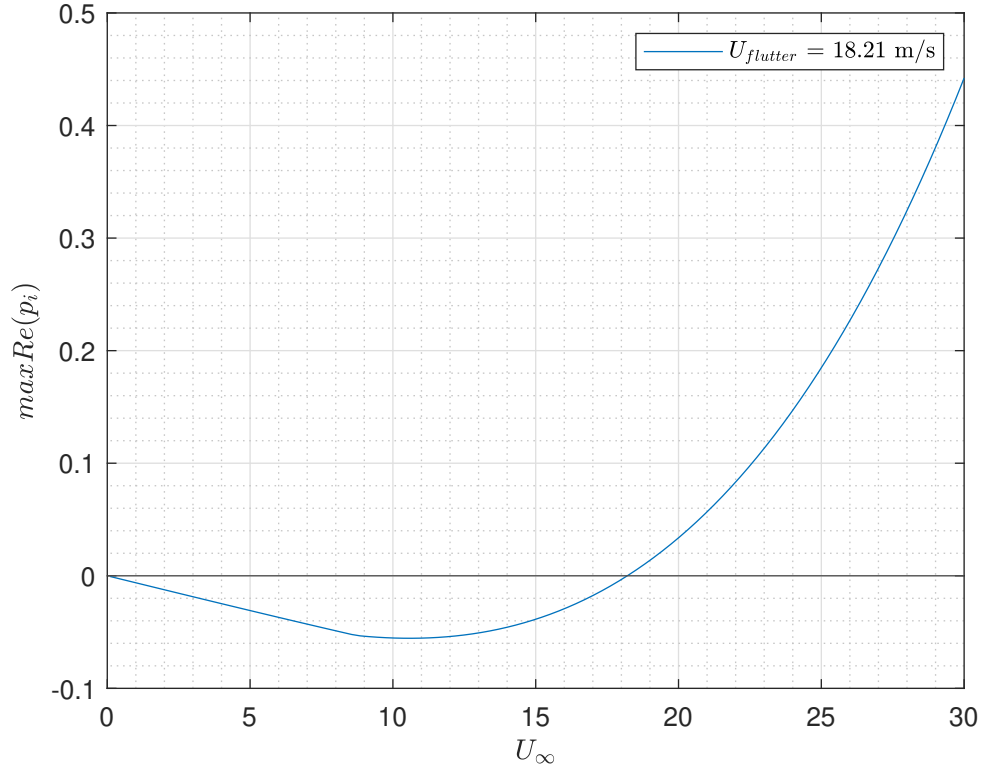


FIGURE 10: Natural modes

To have a better understanding of the specific natural modes that trigger the flutter, the imaginary and real part of the p values of the different modes has been plotted for the different free stream velocities in figure 11. As can be seen, almost all are stable or marginally stable, but the one responsible for starting the flutter is mode 3. This can be easily identified as the plot of $|Im(p_i)|/2\pi$ at 0 velocity matches the natural frequency of the mode.

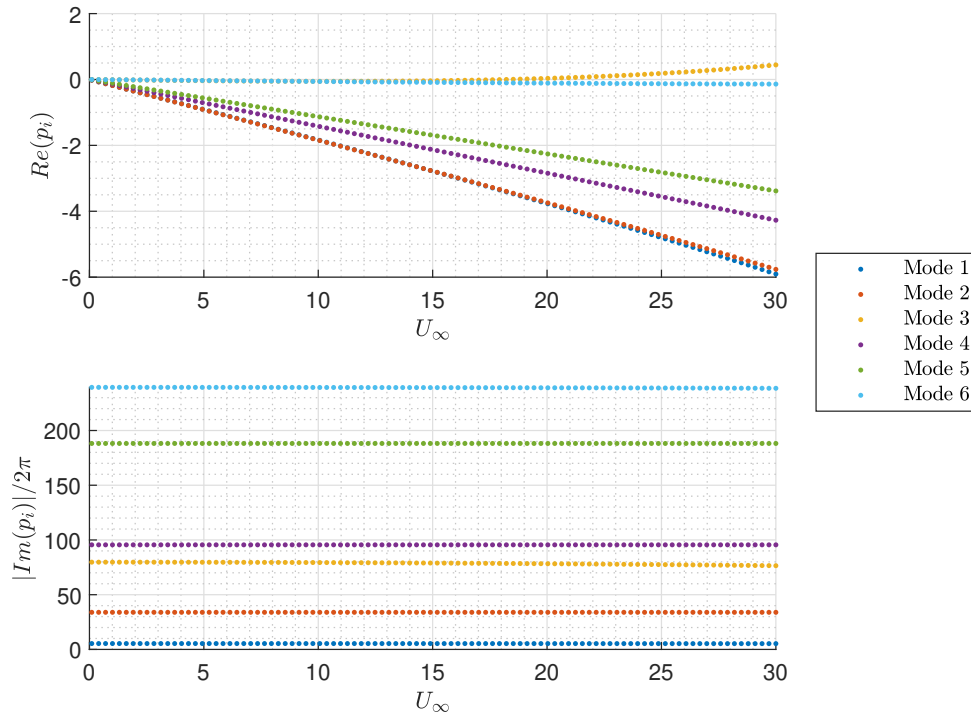


FIGURE 11: Mode's p value evolution

In paper [1] are presented the different flutter initiating velocities that have been obtained in the wind tunnel test of the Pazy Wing. The velocities range from 38 m/s up to 60 m/s, where the calculated one of 18.21 m/s. It is believed that due to the several simplifications that have been commiserated for this numerical method lead to a smaller flutter velocity than the one obtained by actual wind tunnel tests of the Pazy Wing.

TABLE 6: Comparison of test experimental free stream velocity

	Calculated	WT test[1]
U_{∞}^f [m/s]	18.21	38 - 60

5 Conclusions

In this project the Pazy Wing numerical aeroelastic model has been implemented successfully using a quasi steady aerodynamic model and linear structural model. The obtained results disagree up to a certain extend with the literature and actual wind tunnel test of the Pazy Wing porblem, but this is expected since the implemented model is linear and the structure is highly none linear.

Starting with the results for the static response of the structure. It has been observed how the deformations obtained with the aeroelastic coupling lead to larger tip elastic twist and vertical displacement of the structure. The magnitude of the those displacements is coherent and inside the expected outcome.

Regarding the computation of the divergence condition, this one has been obtained solving the inverse eigenvalue problem, since the matrix $[K_a]$ was not possible to invert. This has led to a final divergence velocity of 107 m/s while the literature gets a value of 83 m/s.

The natural modes of vibration of the structure have been calculated and comparing with the modes obtained by the literature, the model developed in this report is missing two modes between second and the third one. Regarding the type of modes obtained, the two first have been the flapping modes and the third one is a torsional mode shape.

Lastly, the flutter condition has also been calculated using the *p-method*. So far, this results have been the ones that had diverged the most from the results from the literature. The calcualted triggering free stream velocity for flutter ahs been of 18 m/s

References

1. DRACHINSKY, Ariel; AVIN, Or; RAVEH, Daniella E; BEN-SHMUEL, Yaron; TUR, Moshe. *Flutter Tests of the Pazy Wing*. Available also from: <https://nescacademy.nasa.gov/workshops/AePW3/public>.
2. RISO, Cristina; CESNIK, Carlos E S. *Investigation of Geometrically Nonlinear Effects in the Aeroelastic Behavior of a Very Flexible Wing*. 2023. Available also from: <https://www.researchgate.net/publication/366186882>.